Direct Numerical Simulation Database for Supersonic and Hypersonic Turbulent Boundary Layers

Chao Zhang[*] and Lian Duan[†]
Missouri University of Science and Technology, Rolla, Missouri 65409
and
Meelan M. Choudhari[‡]
NASA Langley Research Center, Hampton, Virginia 23681

This paper presents a direct numerical simulation database of high-speed zero-pressure-gradient turbulent boundary layers developing spatially over a flat plate with nominal freestream Mach number ranging from 2.5 to 14 and wall-to-recovery temperature ranging from 0.18 to 1.0. The flow conditions of the DNS are representative of the operational conditions of the Purdue Mach 6 quiet tunnel, the Sandia Hypersonic Wind Tunnel at Mach 8, and the AEDC Hypervelocity Tunnel No. 9 at Mach 14. The DNS database is used to gauge the performance of compressibility transformations, including the classical Morkovin's scaling and strong Reynolds analogy as well as the newly proposed mean velocity and temperature scalings that explicitly account for wall heat flux. Several insights into the effect of direct compressibility are gained by inspecting the thermodynamic fluctuations and the Reynolds stress budget terms. Precomputed flow statistics, including Reynolds stresses and their budgets, will be available at the website of the NASA Langley Turbulence Modeling Resource, allowing other investigators to query any property of interest.

Nomenclature

a	=	speed of sound, m/s
B_q	=	wall heat transfer rate, $q_w/(\rho_w C_p u_\tau T_w)$, dimensionless
b_{ij}	=	anisotropy tensor, $\overline{\rho u_i'' u_j''}/(2\overline{\rho k}) - (1/3)\delta_{ij}$, dimensionless
C_p	=	heat capacity at constant pressure, J/(K · kg)
C_v	=	heat capacity at constant volume, J/(K · kg)
D	=	viscous diffusion term, Pa/s
H	=	shape factor, $H \equiv \delta^*/\theta$, dimensionless
k	=	turbulent kinetic energy, $k \equiv u_i'' u_i''/2$, J/kg
M	=	Mach number, $M \equiv u/a$, dimensionless
M_t	=	turbulent Mach number, $M_t \equiv \sqrt{\overline{u_i' u_i'}}/\bar{a}$, dimensionless
M_τ	=	friction Mach number, $u_\tau/(\gamma R T_w)^{1/2}$, dimensionless
N_f	=	number of fields used to accumulate statistics, dimensionless
P	=	production term, Pa/s
Pr	=	molecular Prandtl number, 0.71, dimensionless
Pr_t	=	turbulent Prandtl number, $Pr_t \equiv (\overline{\rho u'w'}(\partial \overline{T}/\partial z))/(\overline{\rho w'T'}(\partial \bar{u}/\partial z))$, dimensionless
p	=	pressure, Pa
q	=	surface heat flux, W/m²
R	=	ideal gas constant, 287, J/(K · kg)
Re_θ	=	Reynolds number based on momentum thickness and freestream viscosity, $Re_\theta \equiv \rho_\infty u_\infty \theta/\mu_\infty$, dimensionless
$Re_{\delta 2}$	=	Reynolds number based on momentum thickness and wall viscosity, $Re_{\delta_2} \equiv \rho_\infty u_\infty \theta/\mu_w$, dimensionless
Re_τ	=	Reynolds number based on shear velocity and wall viscosity, $Re_\tau \equiv \rho_w u_\tau \delta/\mu_w$, dimensionless
Re_τ^*	=	semilocal Reynolds number, $Re_\tau^* \equiv \sqrt{\tau_w/\rho_\infty}\delta/\nu_\infty$, dimensionless
s	=	entropy, J/(kg · K)
ST	=	terms arise when density is not constant, Pa/s
T	=	temperature, K
TT	=	turbulent transport term, Pa/s
T_r	=	recovery temperature, $T_\infty(1 + 0.89((\gamma - 1)/2)M_\infty^2)$, K
T_f	=	time spanned to accumulate statistics, s
U_∞	=	freestream velocity, m/s
u	=	streamwise velocity, m/s
u_τ	=	friction velocity, $u_\tau \equiv \sqrt{\tau_w/\bar{\rho}_w}$, m/s
u^*	=	density weighted velocity scale, $u^* \equiv \sqrt{\tau_w/\bar{\rho}} = u_\tau \sqrt{\bar{\rho}_w/\bar{\rho}}$, m/s
v	=	spanwise velocity, m/s
w	=	wall-normal velocity, m/s
x	=	streamwise direction of the right-handed Cartesian coordinate, m
x_a	=	streamwise location selected for statistical analysis, m
y	=	spanwise direction of the right-handed Cartesian coordinate, m
z	=	wall-normal direction of the right-handed Cartesian coordinate, m
z_τ	=	viscous length, ν_w/u_τ, m
z_τ^*	=	semilocal length scale, $z_\tau^* \equiv \bar{\mu}/(\bar{\rho}u^*)$, m
γ	=	specific heat ratio, C_p/C_v, dimensionless
δ	=	boundary-layer thickness (based on 99% of the freestream velocity), m
δ_{ij}	=	Kronecker delta, dimensionless
δ^*	=	displacement thickness, m
κ	=	von Kármán constant 0.41, dimensionless
ω	=	vorticity, Hz
θ	=	momentum thickness, m
μ	=	dynamic viscosity, $1.458 \times 10^{-6} T^{3/2}/(T + 110.4)$, kg/(m · s)
ν	=	kinematic viscosity, μ/ρ, m²/s
ρ	=	density, kg/m³
τ_w	=	wall shear stress, Pa
τ_{ij}	=	viscous stress tensor, Pa
Π^t	=	pressure diffusion term, Pa/s
Π^d	=	pressure dilatation term, Pa/s
Π^c	=	compressibility term, Pa/s
ϕ	=	viscous dissipation per unit volume, Pa/s

*Graduate Research Assistant, Department of Mechanical and Aerospace Engineering.

†Assistant Professor, Department of Mechanical and Aerospace Engineering. Senior Member AIAA.

‡Aerospace Technologist, Computational Aerosciences Branch, Mail Stop 128. Associate Fellow AIAA.

Subscripts

i	=	inflow station for the domain of direct numerical simulations
rms	=	root mean square
TL	=	variable associated with the transformation of Trettel and Larsson
VD	=	variable associated with Van Driest transformation
w	=	wall variables
∞	=	freestream variables
0	=	stagnation quantities

Superscripts

$+$	=	variable in inner wall units, $(\cdot)^+ \equiv (\cdot)/z_\tau$
$*$	=	variable in semilocal units, $(\cdot)^* \equiv (\cdot)/z_\tau^*$
$\overline{(\cdot)}$	=	standard (Reynolds) averaged variable
$\widetilde{(\cdot)}$	=	density-weighted (Favre) averaged variable, $\widetilde{(\cdot)} \equiv \overline{\rho(\cdot)}/\bar{\rho}$
$(\cdot)'$	=	fluctuations around standard averages
$(\cdot)''$	=	fluctuations around Favre averages

I. Introduction

THE knowledge of turbulent boundary layers at high Mach numbers is important to the design of high-speed vehicles, as turbulent boundary layers determine the aerodynamic drag and heat transfer. One of the most important foundations for our understanding of high-speed turbulence is Morkovin's hypothesis, which postulates that high-speed turbulence structure in zero pressure-gradient turbulent boundary layers remains largely the same as its incompressible counterpart [1]. An important consequence of Morkovin's hypothesis is the so-called "compressibility transformations" that transform the mean velocity and Reynolds stress profiles in a compressible boundary layer to equivalent incompressible profiles by accounting for mean property variations across the thickness of the boundary layer. A classic example of such transformations is the density-weighted velocity scaling of Van Driest [2]. Another consequence of Morkovin's hypothesis is the analogy between the temperature and velocity fields that leads to velocity-temperature relations such as the classical Walz formula [3] and the strong Reynolds numbers analogy (SRA) [4–6]. In addition to the classical Van Driest transformation and the SRA, which have been verified largely for supersonic turbulent boundary layers ($M_\infty < 5$) with an adiabatic wall, new mean velocity and velocity-temperature scaling relations have recently been proposed to explicitly account for a finite wall heat flux [7–9]. For example, Patel et al. [10] proposed a semilocal Reynolds number Re_τ^* for comparing wall turbulence statistics among cases with substantially different mean density and viscosity profiles. Trettel and Larsson [7] recently provided an extension to the Van Driest transformation for compressible wall turbulence with heat transfer by deriving a novel velocity transformation based on arguments about log-layer scaling and near-wall momentum conservation. Zhang et al. [8] generalized the temperature-velocity relation of Walz and Huang's SRA to explicitly account for a finite wall heat flux. These new scaling relations have been shown to yield much improved collapse of the supersonic data to the incompressible case when there is a strong heat transfer at the surface [11]. The success of the compressibility transformations and the SRA may suggest that there exist few, if any, dynamic differences due to Mach number, as postulated by Morkovin, at least for wall turbulence at moderate Mach numbers ($M_\infty < 5$).

At hypersonic speeds ($M_\infty > 5$), the validity of Morkovin's hypothesis may come into question because of the increasing density and pressure fluctuations at high Mach numbers. Turbulent fluctuations can even become locally supersonic relative to the surrounding flow, creating the so-called eddy shocklets that could significantly modify the dynamics of the flow. However, the Mach number at which Morkovin's hypothesis would lose significant accuracy remains largely undetermined. There are still limited measurements at hypersonic speeds that are detailed and accurate enough for testing the validity of Morkovin's hypothesis.

Experimental investigations of hypersonic turbulent boundary layers have been conducted historically with hot-wire anemometry (see, for example, the review by Roy and Blottner [12]). A recent investigation by Williams et al. [13] showed that much of the historical hot-wire measurements of turbulence statistics suffered from poor frequency response and/or spatial resolution. Hot-wire anemometry may also suffer from uncertainties associated with the mixed-mode sensitivity of the hot wires, given that the hot wire measures a combination of the fluctuating mass flux and the fluctuating total temperature [14]. In addition to hot-wire anemometry, direct measurements of spatially varying velocity fields of high-speed turbulent boundary layers have been attempted using particle image velocimetry (PIV) [13,15–17]. Among the existing PIV measurements, the measurement by Williams et al. [13] in a Mach 7.5 flat-plate turbulent boundary layer is the only PIV measurement conducted at a Mach number above 5. Although the existing PIV results provided direct experimental evidence for the validity of Morkovin scaling for the streamwise velocity at Mach numbers as high as 7.5, accurate measurements were not yet acquired for the wall-normal component of the velocity or the Reynolds stress. The existing PIV data exhibited reduced levels of the wall-normal component of the velocity in comparison with the predictions based on the Morkovin scaling, and the deviation became larger with increasing Mach number. As noticed by Williams et al. [13], the loss in accuracy is largely due to particle response limitations that result in significantly reduced levels of wall-normal velocity fluctuations.

Complementary to experiments, direct numerical simulations (DNS) of high-speed turbulent boundary layers have been conducted to overcome the experimental difficulties and provide access to three-dimensional turbulence statistics. Although several DNS have been conducted for studying Morkovin's scaling in turbulent boundary layers with moderate freestream Mach number ($M < 5$) [7,8,11, 18–22], there is little DNS data for turbulent boundary layers in the high-Mach-number regime [12]. Martín [23,24] made a pioneering effort toward characterizing boundary-layer turbulence in the hypersonic regime by developing a temporal DNS database of canonical zero-pressure-gradient, flat-plate turbulent boundary layers up to Mach 8 with varying wall temperatures. Duan et al. [25–27] extended the datasets of Martín [23] to even higher Mach numbers (up to Mach 12) with cold wall and high enthalpy and conducted a systematic study of wall turbulence and its dependence on freestream Mach number, wall cooling, and high enthalpy. Additional DNS studies of hypersonic turbulent boundary layers in the literature include that by Lagha et al. [28] up to Mach 20 with an adiabatic wall ($T_w/T_r = 1.0$) and that by Priebe and Martín at Mach 7.2 [29] with $T_w/T_r = 0.53$. Except for the work by Duan et al. [26], who systematically studied the effect of wall cooling on boundary-layer turbulence at Mach 5, most of the previous DNS at high Mach number simulated a turbulent boundary layer over a hypothetically adiabatic wall. The new scaling relations of Refs. [7–9] that explicitly account for finite wall heat flux have not yet been systematically assessed under high Mach number, cold-wall conditions.

As far as the modeling of high-speed turbulence is concerned, the most common classes of compressibility correction for Reynolds-averaged Navier–Stokes (RANS) turbulence models were developed for improving predictions of free-shear layers or jets. As such, these corrections are often unacceptable for attached boundary-layer flows. However, practical experiences indicate that the need for correction in hypersonic boundary layers becomes increasingly evident as Mach number increases, particularly for cold walls [30,31]. In particular, Rumsey [31] recently investigated the performance of many of the compressibility corrections described in the literature for $k - \omega$ turbulence models in hypersonic boundary-layer applications. He found that the dilatation-dissipation correction designed by Zeman [30] works reasonably well for predicting turbulent skin friction at high-Mach-number, cold wall conditions. As concluded by Rumsey, the effects of dilatation-dissipation and pressure-dilation on turbulence models are still not clear for high-Mach-number, cold wall cases, and there is a need for improved understanding and better physical modeling for turbulence models applied to hypersonic boundary layers.

In the present paper, we describe a new DNS database of spatially developing, flat-plate turbulent boundary layers that was developed using a large computational domain with low-dissipative spatial discretization, and that covers a wide range of freestream Mach number ($M_\infty = 2.5\text{–}14$) and wall-to-recovery temperature ratio ($T_w/T_r = 0.18\text{–}1.0$). Unlike the temporal DNS of Martín [23] and Duan et al. [25,26] that used a small streamwise domain ($\approx 8\delta$) with a periodic boundary condition in the streamwise direction, these DNS simulate spatially developing turbulent boundary layers with a long streamwise domain length ($> 50\delta_i$) to minimize any artificial effects of inflow turbulence generation and to guarantee the convergence of high-order turbulence statistics. Moreover, the new DNS database mimics realistic flow conditions such as those in hypersonic wind tunnel facilities with a cooled wall rather than simulating hypersonic turbulent boundary layers over a hypothetically adiabatic wall [24,25,28]. The combination of high freestream Mach number (with nominal freestream Mach number as high as $M_\infty = 14$) and cold wall temperature (with wall-to-recovery temperature as low as $T_w/T_r = 0.18$) covered in the database extends the available database to more extreme, yet practical, cases that serve as a reference for modeling wall-bounded turbulence in the high-Mach-number, cold-wall regime as well as for developing novel compressibility transformations that collapse compressible boundary-layer profiles to incompressible results. For that purpose, both statistical quantities and subsets of raw flow samples are made publicly available on a website, which will allow other investigators to access any property of interest. In the following sections, we briefly describe the DNS methodology and present a limited number of numerical results, including a comparison with recent experimental data and an application of the numerical data to gauge the performance of some recently proposed compressibility transformations [7,8] and to probe intrinsic compressibility effects.

II. Numerical Database and Underlying Methodology

The database used for the current analysis includes the DNS of spatially developing, flat-plate turbulent boundary layers over a wide range of nominal freestream Mach numbers ($M_\infty = 2.5\text{–}14$) and wall-to-recovery temperature ratios ($T_w/T_r = 0.18\text{–}1.0$). Table 1 outlines the freestream conditions for the simulations, and Table 2 summarizes the boundary-layer parameters at a selected location where the turbulence statistics are gathered. Cases M2p5, M6Tw076, and M6Tw025 correspond to the DNS reported in previous papers [32–35], in which pressure statistics including the freestream acoustic radiation were presented and discussed in detail. The flow conditions of case M2p5 match those of the temporal simulation of Guarini et al. [36]; case M6Tw076 simulates representative conditions of the Purdue Mach 6 Quiet Tunnel; case M6Tw025 has nearly identical flow conditions as the wind-tunnel relevant case M6Tw076 while varying the surface temperature ratio T_w/T_r from

0.76 to 0.25 to allow an assessment of the effect of surface temperature. Two additional cases at higher freestream Mach numbers (cases M8Tw048 and M14Tw018) are presented herein for the first time, with flow conditions representative of the nozzle exit of the Sandia Hypersonic Wind Tunnel at Mach 8 and the AEDC Hypervelocity Tunnel No. 9 at Mach 14, respectively. The new cases extend the available database to more extreme, yet practical, cases that would allow one to probe the effects of Mach number on turbulence scaling and structure under these conditions. Choosing flow conditions that are representative of several hypersonic wind tunnels has led to successful one-to-one comparisons of the DNS with experimental measurements in these wind tunnels [37]. As much as possible, the Re_τ parameter is kept within the narrow range of 450–500, the only exception being the Mach 14 case, where the Re_τ increased because a longer spatial domain was necessary to ensure that the effects of inflow treatment had decayed and the boundary layer had achieved a quasi-equilibrium state. The decision to match Re_τ is based on the existing literature [28,38] as well as on the need to limit the computational costs even though simulations at a single Reynolds number may not be sufficient to characterize the flow [39,40]. All the DNS cases fall within the perfect gas regime. The working fluid is air with viscosity calculated by using Sutherland's law, except for case M8Tw048, where the working fluid is nitrogen and its viscosity is calculated by using Keyes law [41]. Compared with the large differences in boundary-layer properties caused by varying the freestream Mach number and the wall temperature, the differences caused by using a different working fluid in DNS are small, if not negligible. A constant molecular Prandtl number of 0.71 is used for all of the DNS cases.

Table 3 summarizes the domain sizes and grid resolutions for all DNS cases. The simulations either involve a single domain with a long streamwise box or are carried out in two stages involving overlapping streamwise domains as illustrated in Fig. 1. The boundary layer is allowed to develop spatially over an extended region along the streamwise direction ($> 50\delta_i$) so as to minimize any artificial effects of the inflow turbulence generation and to contain the largest relevant flow structures within the computational domain. The two overlapping streamwise domains used in case M14Tw018 further minimize any artificial effects of the rescaling procedure. This conservative approach was deemed necessary because of the combination of higher freestream Mach number and colder wall temperature than the other cases considered herein, as well as in other computational studies reported in the literature. Another noteworthy feature of the present database corresponds to the large spanwise domain (nearly an order of magnitude larger than the boundary-layer thickness), which guarantees spanwise statistical decorrelation in turbulence fluctuations throughout the boundary layer.

The boundary layer is simulated in a rectangular box over a flat plate with spanwise periodic boundary conditions and a modified rescaling/recycling method for inflow turbulence generation [32].

Table 1   Freestream and wall-temperature conditions for various DNS cases

Case	M_∞	U_∞, m/s	ρ_∞, kg/m³	T_∞, K	T_w, K	T_w/T_r	δ_i, mm
M2p5	2.50	823.6	0.100	270.0	568.0	1.0	4.0
M6Tw025	5.84	869.1	0.044	55.2	97.5	0.25	1.3
M6Tw076	5.86	870.4	0.043	55.0	300.0	0.76	13.8
M8Tw048	7.87	1155.1	0.026	51.8	298.0	0.48	20.0
M14Tw018	13.64	1882.2	0.017	47.4	300.0	0.18	18.8

Table 2   Boundary-layer properties at the station selected for the analysis for various DNS cases

Case	x_a/δ_i	Re_θ	Re_τ	Re_{δ_2}	Re_τ^*	θ, mm	H	δ, mm	z, μm	u_τ, m/s	$-B_q$	M_τ
M2p5	53.0	2835	510	1657	1187	0.58	4.1	7.7	15.0	40.6	0	0.08
M6Tw025	88.6	2121	450	1135	932	0.20	8.4	3.6	8.0	33.8	0.14	0.17
M6Tw076	54.1	9455	453	1746	4130	0.95	13.6	23.8	52.6	45.1	0.02	0.13
M8Tw048	56.9	9714	480	1990	4092	1.19	17.4	35.2	73.5	54.3	0.06	0.15
M14Tw018	199.3	14408	646	2354	4925	1.35	37.6	66.1	102.4	67.6	0.19	0.19

Table 3   Grid resolution and domain size for the direct numerical simulations

Case	$N_x \times N_y \times N_z$	L_x/δ_i	L_y/δ_i	L_z/δ_i	Δx^+	Δy^+	$\Delta z^+_{\min}$	$\Delta z^+_{\max}$	N_f	$T_f u_\tau/\delta$
M2p5	$1760 \times 800 \times 400$	57.2	15.6	41.0	9.2	5.5	0.60	9.5	282	14.9
M6Tw025	$2400 \times 400 \times 560$	91.7	8.8	57.5	6.4	3.7	0.46	4.8	312	7.3
M6Tw076	$1600 \times 800 \times 500$	58.7	15.7	39.7	9.6	5.1	0.51	5.3	153	7.3
M8Tw048	$3200 \times 500 \times 600$	65.0	10.2	41.2	5.4	5.4	0.55	5.6	248	5.7
M14Tw018, Box 1	$2500 \times 460 \times 540$	133.3	12.2	55.6	9.4	4.7	0.47	5.2	—	—
M14Tw018, Box 2	$2000 \times 460 \times 786$	102.1	12.2	55.6	9.4	4.7	0.47	5.7	137	1.4

L_x, L_y, and L_z are the domain size in the streamwise, spanwise, and wall-normal directions, respectively. Δx^+ and Δy^+ are the uniform grid spacing in the streamwise and spanwise directions, respectively; $\Delta z^+_{\min}$ and $\Delta z^+_{\max}$ denote the minimum and maximum wall-normal grid spacing. The grid resolutions are normalized by the viscous length z_τ at the location where the turbulence statistics are gathered. N_f is the number of fields used to accumulate statistics, and T_f is the time spanned by those fields. The values of δ_i, z_τ, u_τ, and δ for each case are listed in Tables 1 and 2. δ_i corresponds to that of Box 1 in case M14Tw018.

The numerical code solves the compressible Navier–Stokes equations in conservative form, using an optimized seventh-order weighted essentially nonoscillatory (WENO) scheme [42,43] for capturing eddy shocklets and ensuring numerical stability. A third-order low-storage Runge–Kutta scheme is used for time integration [44]. A detailed description of the problem formulation, the numerical scheme, and the initial and boundary conditions can be found in Ref. [32–35]. The validity of numerical methods and procedures have been established in multiple previous publications [33,34,45], with the computational domain size and grid resolution summarized in Table 3. The computational grid resolution inside the boundary layer is comparable to those reported in the literature in the context of previous simulations of turbulent wall-bounded flows using comparable numerical algorithms [25,26,32–35]. The effect of spanwise domain size on flow statistics is monitored by sufficient decay of two-point correlations and/or by comparing to cases with an auxiliary simulation of the same grid resolution but with a narrower span, and negligible difference is observed in the flow statistics of interest. Furthermore, the physical realism and accuracy of the computed flow fields have been validated by comparing to experimental results at similar flow conditions [33,37]. Additional comparisons of DNS results with both experiments and other high-quality simulations are presented in the following sections.

In the following sections, averages are first calculated over a streamwise window ($[x_a - 0.9\delta_i, x_a + 0.9\delta_i]$) and the spanwise direction for each instantaneous flow field; then, an ensemble average over N_f flow-field snapshots spanning a time interval of $T_f u_\tau/\delta$ is calculated. Statistical convergence is verified by calculating averages over varying streamwise window sizes or over a different number of snapshots and by making sure that the differences in flow statistics are negligible (<1%) among the different data-averaging techniques. Throughout the paper, statistics are reported based on fluctuations either around the standard (Reynolds) averages or around density-weighted (Favre) averages. For Mach numbers as high as 13.64, only small differences (<3%) have been found between the standard and density-weighted (Favre) averages for the statistics reported in this paper.

III.   Computational Results

A.   Compressibility Transformations

In this section, the DNS database is used to gauge the performance of several velocity and temperature scalings. Complementary to the previous studies of Duan et al. [25,26], the present study pays special attention to the recently proposed scaling relations [7,8,10] that have not yet been scrutinized in the high-Mach-number, cold-wall regime, in addition to the classical scalings according to Morkovin.

Figure 2 plots the Van Driest transformed mean velocity u^+_{VD}, which is defined as

$$u^+_{\mathrm{VD}} = \frac{1}{u_\tau} \int_0^{\bar{u}} (\bar{\rho}/\bar{\rho}_w)^{1/2} \, d\bar{u} \qquad (1)$$

The mean velocity shows an approximately logarithmic region where $u^+_{\mathrm{VD}} = (1/k) \log(z^+) + C_{\mathrm{VD}}$ upon Van Driest transformation. The Van Driest transformed mean velocity shows a decrease in the mean slope S_{VD} in the linear viscous sublayer with higher wall

a) M8Tw048   **b) M14Tw018**
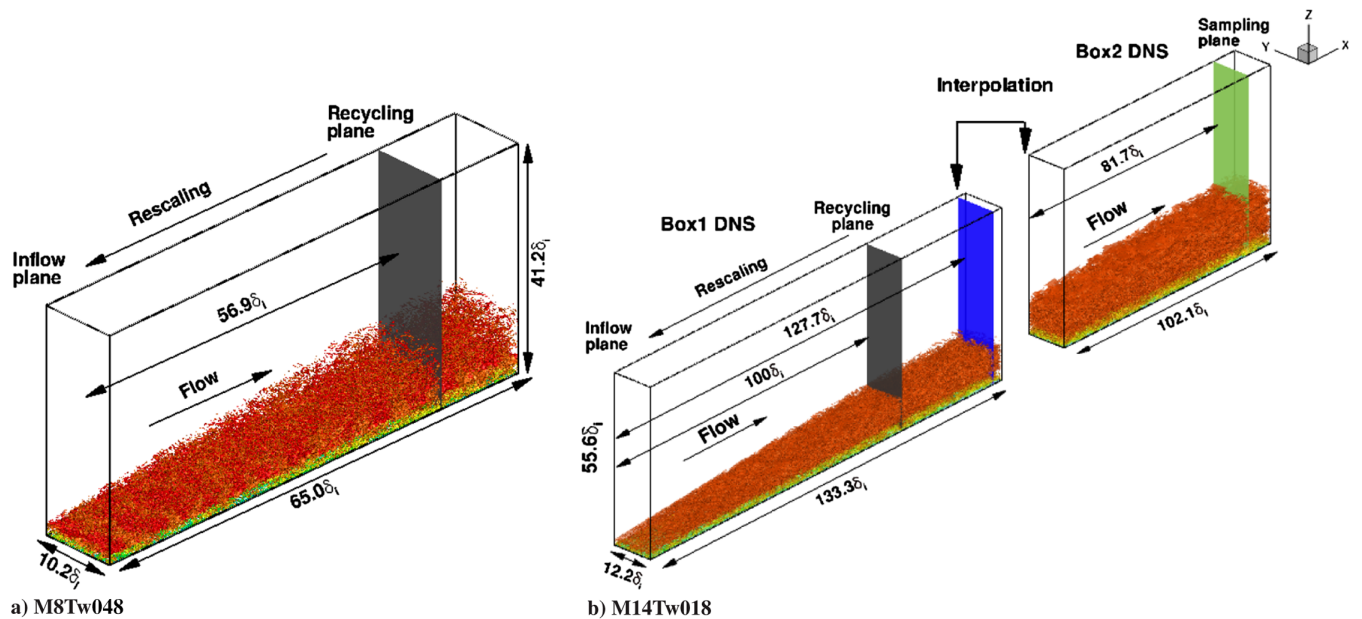
Fig. 1   Computational domain and simulation setup for DNS of Mach 8 and Mach 14 turbulent boundary layers, with flow conditions representative of the nozzle exit of the Sandia Hypersonic Wind Tunnel at Mach 8 and the AEDC Hypervelocity Tunnel No. 9 at Mach 14, respectively. An instantaneous flowfield is shown, visualized by an isosurface of the density gradient magnitude, corresponding to $|\nabla\rho|\delta_i/\rho_\infty = 0.9825$, colored by the streamwise velocity component (with levels from 0 to U_∞, blue to red).
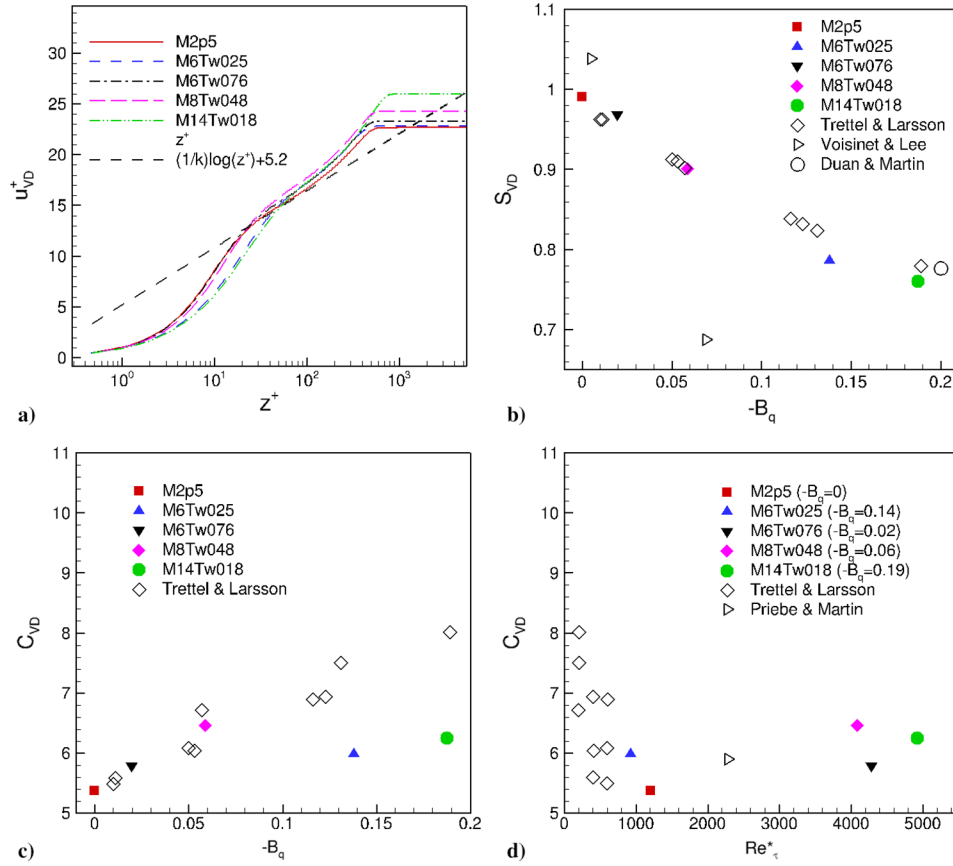
Fig. 2 Effect of applying the Van Driest transformation to the mean velocity profile. a) Velocity profile u_{VD}^+; b) viscous sublayer slope S_{VD}; c) log-law intercept C_{VD} as functions of the wall-cooling rate $-B_q$; d) Reynolds number effects in the log-law intercept C_{VD}.

cooling rate $-B_q$. A similar trend was reported in previous studies of Refs. [11,26,34,38,46]. The log-layer intercept C_{VD} slightly increases with wall-cooling rate and Reynolds number, although the change seems to be less rapid in comparison with the results for compressible channel flows with cooled walls [7,47,48] and a turbulent boundary layer at Mach 4.5 [18]. Here, we use the semilocal Reynolds number Re_τ^* as a characteristic Reynolds number for comparing C_{VD} among the different DNS cases, since Re_τ^* is known from Patel et al. [10] to be the governing parameter for wall turbulence statistics with different mean density and viscosity profiles, at least for wall turbulence at lower Mach numbers.

An alternative transformation of mean velocity was proposed by Trettel and Larsson [7] for compressible wall turbulence with cold walls, based on arguments about log-layer scaling and near-wall momentum conservation. The velocity scaling is defined as

$$u_{\mathrm{TL}}^+ = \int_0^{u^+} \left(\frac{\bar{\rho}}{\rho_w}\right)^{1/2} \left[1 + \frac{1}{2}\frac{1}{\bar{\rho}}\frac{d\bar{\rho}}{dz}z - \frac{1}{\bar{\mu}}\frac{d\bar{\mu}}{dz}z\right] du^+ \qquad (2)$$

Figure 3 shows a much improved collapse within the viscous sublayer region of the computational datasets when the modified velocity u_{TL}^+ is used for comparison. Furthermore, the sublayer slope S_{TL} of the transformed velocity is nearly constant at different wall-cooling rates. The collapse of u_{TL}^+ in the viscous sublayer is not unexpected, because the velocity transformation of Trettel and Larsson [7] is designed to satisfy the stress-balance condition within the entire inner layer, including the viscous sublayer. In the log region, however, the log-law intercept C_{TL} of the transformed velocity u_{TL}^+ shows a similar scatter as that of the Van Driest transformed velocity at different wall-cooling rates and Reynolds numbers, and the value of C_{TL} for boundary layers is consistently larger than that for channel flows. The difference in the log-law intercept between boundary layers and channels may suggest an influence of the "wake" component on the log region for boundary

layers. The lack of collapse in C_{TL} for boundary layers may also be due to the discrepancy in the characteristic Reynolds number Re_τ^* among the boundary-layer DNS cases or a lack of an extended log-law region for the existing boundary-layer datasets, making it difficult to accurately probe the log-law region. Although not shown here, a different mean velocity transformation proposed by Patel et al. [9] based on Re_τ^* gives very similar results as that of Trettel and Larsson [7].

Figure 4 plots the wall-normal profiles of the turbulence intensities and the Reynolds shear stress. In general, an apparently good collapse of the data across a wide range of Mach numbers is achieved via Morkovin's scaling [4], consistent with the experimental and computational observations of Refs. [13,17,25,26] at lower Mach numbers and/or without strong wall cooling. The wall-normal component of turbulence intensity and the Reynolds stress measured by PIV [13] exhibit reduced magnitude than those predicted by the various DNS at high Mach number. Such a reduction in magnitude is typical of particle-based velocimetry studies of supersonic flows [13]. Figures 5 and 6 further show that the peak locations of turbulence intensities and the Reynolds shear stress in the classical inner scaling (z^+) shift away from the wall with increasing wall-cooling rate. The semilocal scaling (z^*) of Huang et al. [6] better collapses the location of the near-wall peak of turbulence intensities and the Reynolds shear stress. There is an apparent increase in the peak value of the Morkovin transformed streamwise turbulence intensity u'_{rms}/u^* as the freestream Mach number increases, which is consistent with the DNS of turbulent channel flows at bulk Mach numbers of 1.5 and 3 by Modesti and Pirozzoli [11]. A similar increase in the near-wall peak value with increasing Mach number is not observed for the spanwise and wall-normal turbulence intensities or for the Reynolds shear stress. Away from the wall in the outer layer, the semilocal scaling appears to exaggerate the discrepancy among the different cases, while the outer scaling (z/δ) would better collapse the data as suggested in Fig. 4.
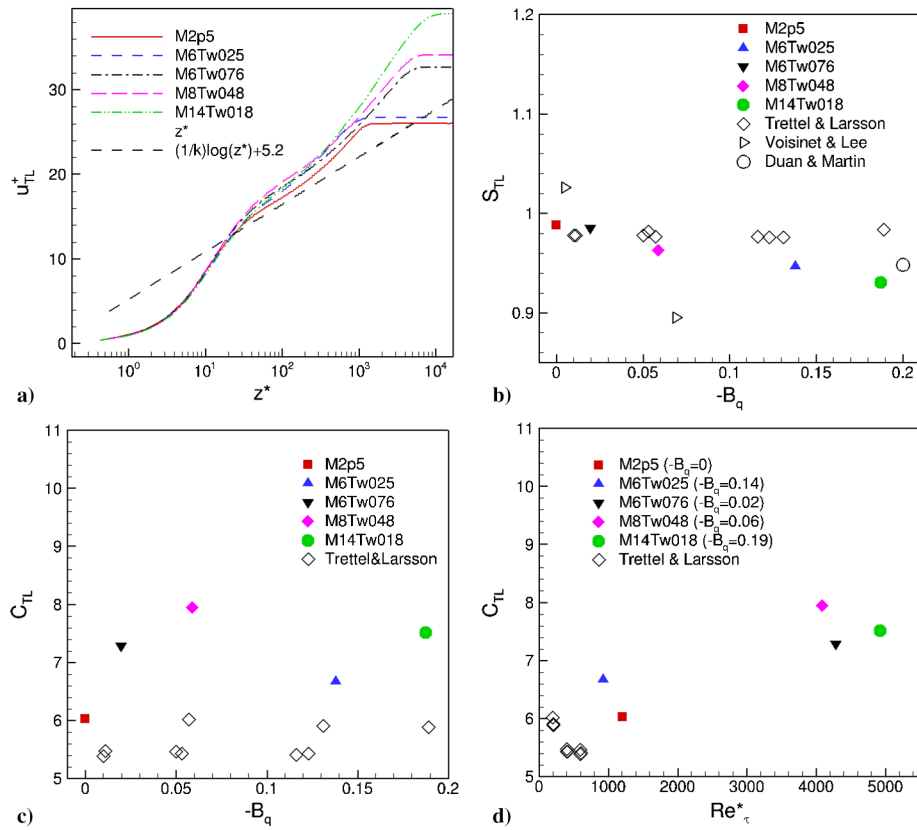
Fig. 3 **Effect of applying the Trettel and Larsson [7] transformation to the mean velocity profile. a) Velocity profile u_{TL}^+; b) viscous sublayer slope S_{TL}; c) log-law intercept C_{TL} as functions of the wall-cooling rate $-B_q$; d) Reynolds number effects in the log-law intercept C_{TL}. The open diamonds denote the results for compressible turbulent channels by Trettel and Larsson [7].**
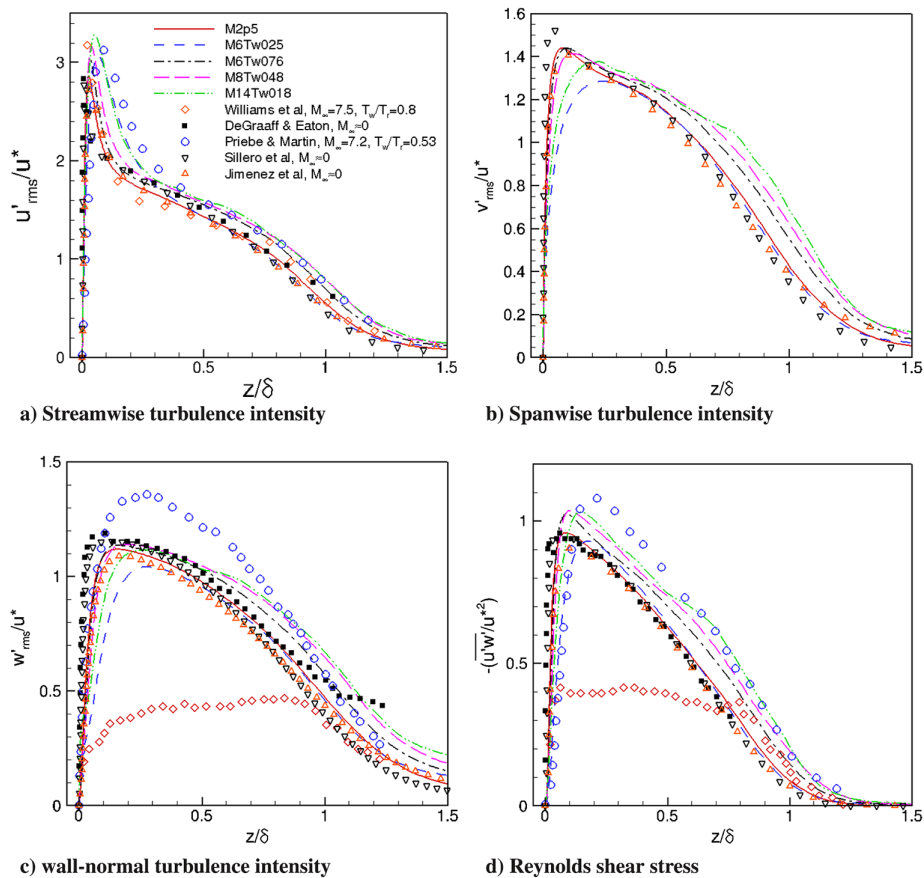
Fig. 4 **Turbulence intensities and Reynolds shear stress transformed according to Morkovin as a function of wall-normal distance z/δ, where $u^* = u_\tau \sqrt{\bar{\rho}_w/\bar{\rho}}$ is the Morkovin transformed velocity scale. For comparison, experimental data by Williams et al. [13] ($M_\infty = 7.5$, $Re_\tau = 279$, $T_w/T_r = 0.8$) and DeGraaff and Eaton [49] ($M_\infty \approx 0$, $Re_\tau = 2220$) along with DNS data by Priebe and Martín [29] ($M_\infty = 7.2$, $Re_\tau = 233$, $T_w/T_r = 0.53$), Sillero et al. [50] ($M_\infty \approx 0$, $Re_\tau = 1310$), and Jiménez et al. [51] ($M_\infty \approx 0$, $Re_\tau = 445$) are also plotted in this figures.**
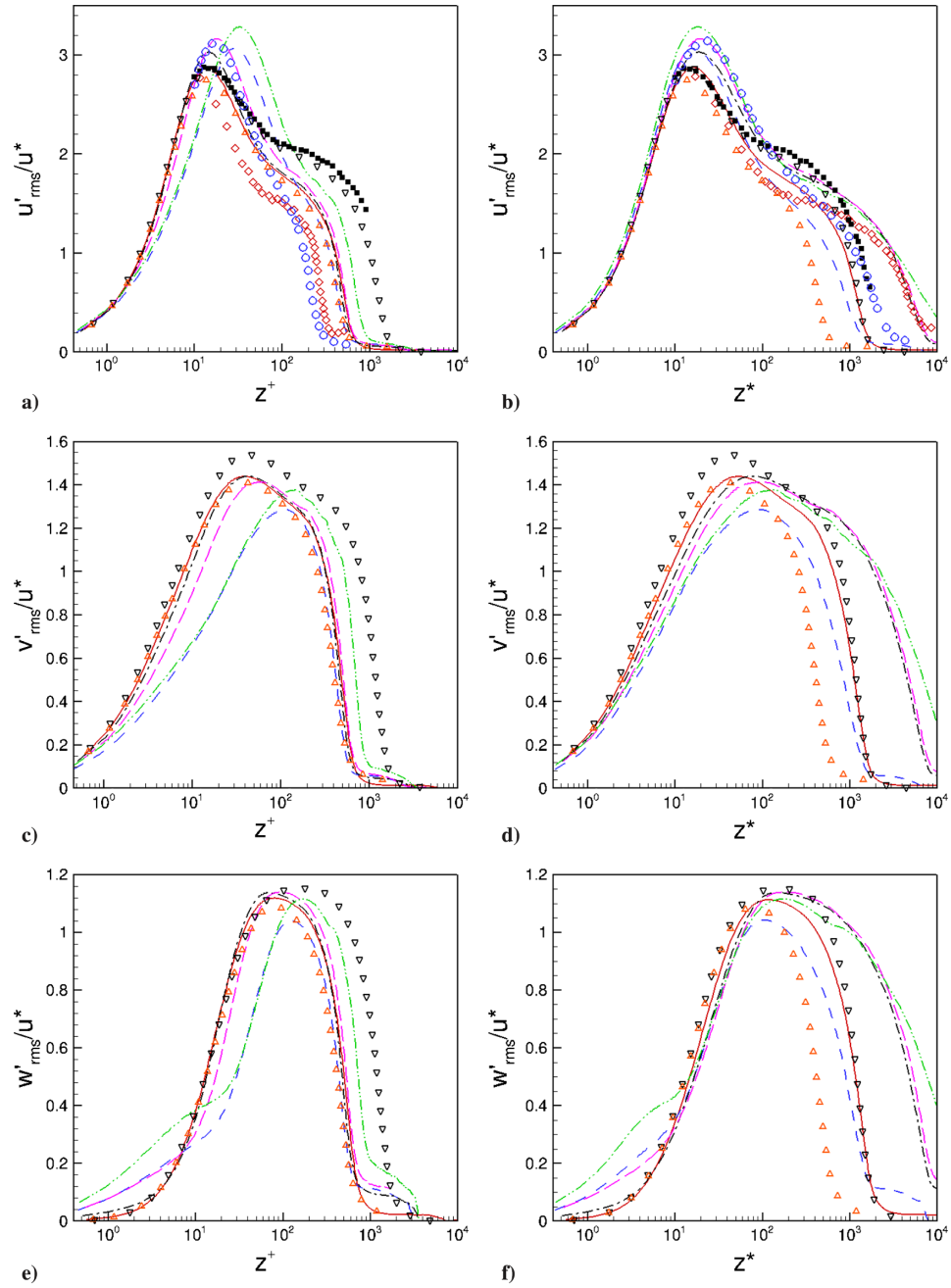
Fig. 5   Turbulence intensities transformed according to Morkovin in (a, c, e) classical inner scaling and (b, d, f) semilocal scaling. See Fig. 4 for symbol legend.
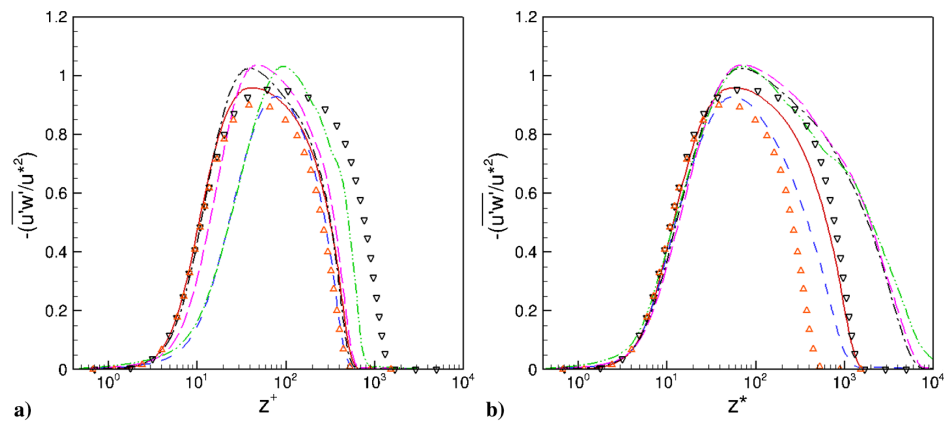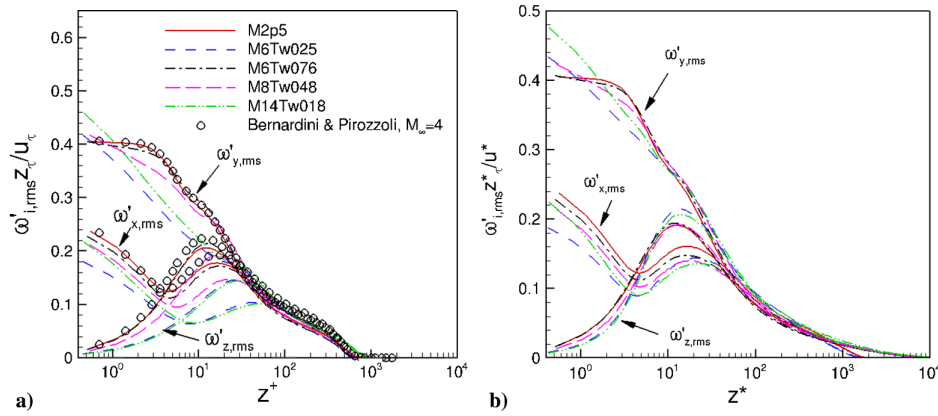

Fig. 6   Reynolds shear stress transformed according to Morkovin in a) classical inner scaling and b) semilocal scaling. See Fig. 4 for symbol legend.

Fig. 7   Wall-normal distribution of vorticity fluctuations nondimensionalized by a) wall units and b) semilocal units, respectively. Variable in wall units are normalized by u_τ/z_τ, and variables in semilocal units are normalized by u^*/z_τ^*. For comparison, the DNS data by Bernardini and Pirozzoli [52] ($M_\infty = 4$, $T_w/T_r = 1$, $Re_\tau = 500$) is also plotted in (a).

The vorticity fluctuation components are presented in Figs. 7a and 7b, scaled in wall units and semilocal units, respectively. Excellent comparison in vorticity fluctuations is achieved between case M2p5 of the current DNS and the DNS of Bernardini and Pirozzoli [52] at Mach 4 with an adiabatic wall. The semilocal scaling yields a much improved collapse of vorticity fluctuation distributions among the DNS cases in most parts of the boundary layer, although notable differences exist in $z^* \lesssim 10$ for the spanwise vorticity component and in $z^* \lesssim 30$ for the streamwise and wall-normal components. Because the vorticity fluctuations are largely induced by small-scale turbulence motions, the better collapse of vorticity profiles among the various DNS cases with semilocal scaling may indicate that the small scale motions are dictated by local mean flow conditions in terms of the mean density and the mean viscosity. A similar observation has been made by Modesti and Pirozzoli [11] in their DNS study of compressible isothermal channel flow at bulk Mach numbers of 1.5 and 3. Furthermore, the differences in semilocally scaled vorticity fluctuations $\omega'_{i,rms}z_\tau^*/u^*$ within the near-wall region among the various DNS cases may be due to wall temperature effects that cause a change in turbulence anisotropy, as a similar variation in the near-wall vorticity fluctuations has also been reported by Patel et al. [9] in the context of zero-Mach-number channel flows with different surface heat transfer rates. The changes in turbulence anisotropy in the near-wall region are also indicated by Fig. 13 in Sec. III.C.

As far as the coupling between thermal and velocity fields is concerned, Fig. 8 plots the mean temperature as a function of the mean velocity for the two highest-Mach-number DNS cases (M8Tw048 and M14Tw018). The DNS results are compared with the classical relation of Walz [3] and a modified relation of Zhang et al. [8]. The Walz relation compares reasonably well with the DNS data

for case M8Tw048, whereas a significantly larger deviation from DNS exists for case M14Tw018. The modified version of Zhang et al. [8], which explicitly accounts for the finite wall heat flux, leads to a much improved comparison with the DNS at Mach numbers as high as 14.

Figure 9 shows the turbulent Prandtl number Pr_t and the modified SRA of Huang et al. [6] across the boundary layer. The Huang's SRA (HSRA) relates the temperature fluctuations T'_{rms} to the streamwise velocity fluctuations u'_{rms} as given by

$$\frac{T'_{rms}/\bar{T}}{(\gamma - 1)M^2(u'_{rms}/\bar{u})} = \frac{1}{Pr_t(1 - (\partial\bar{T}_t/\partial\bar{T}))} \tag{3}$$

The results from Fig. 9 suggest that both Pr_t and HSRA are insensitive to the freestream Mach number and the wall temperature conditions, with values close to unity in most of the outer region of the boundary layer. Although not shown here, a different modified SRA recently proposed by Zhang et al. [8] gives marginally improved prediction compared with HSRA for $z/\delta < 0.8$. The temperature-velocity scalings as high as Mach 13.64 are generally consistent with the predictions from several previous studies at lower Mach numbers [8,26,38].

B.   Thermodynamic Properties

In this section, several thermodynamic fluctuations and their dependence on Mach number and wall temperature conditions are presented. Thermodynamic fluctuations, especially the density fluctuations, appear in many unclosed terms in the RANS equations, the knowledge of which is thus useful for turbulence modeling.
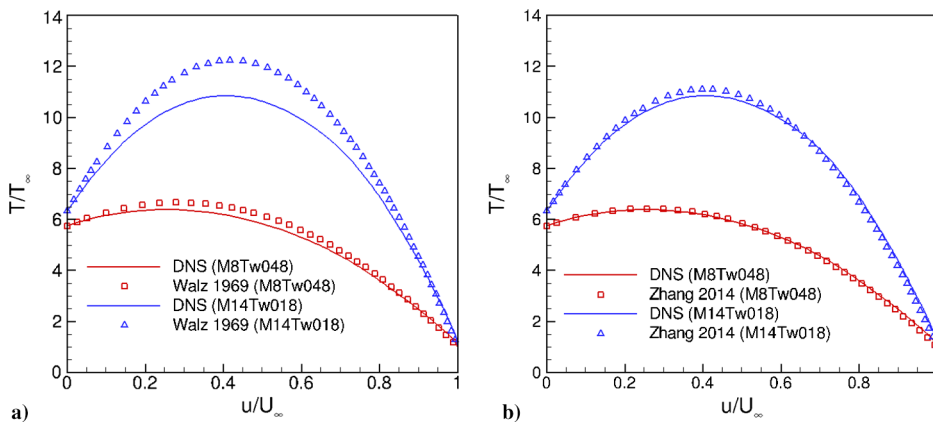
Fig. 8   Relation between mean temperature and mean velocity. a) The classical relation of Walz [3]: $\bar{T}/T_\infty = T_w/T_\infty + ((T_r - T_w)/T_\infty)(\bar{u}/U_\infty) + ((T_\infty - T_r)/T_\infty)(\bar{u}/U_\infty)^2$; b) the generalized relation of Zhang et al. [8]: $\bar{T}/T_\infty = T_w/T_\infty + ((T_{rg} - T_w)/T_\infty)(\bar{u}/U_\infty) + ((T_\infty - T_{rg})/T_\infty)(\bar{u}/U_\infty)^2$, where $T_{rg} = T_\infty + r_g U_\infty^2/(2C_p)$ and $r_g = 2C_p(T_w - T_\infty)/U_\infty^2 - 2Prq_w/(U_\infty\tau_w)$.
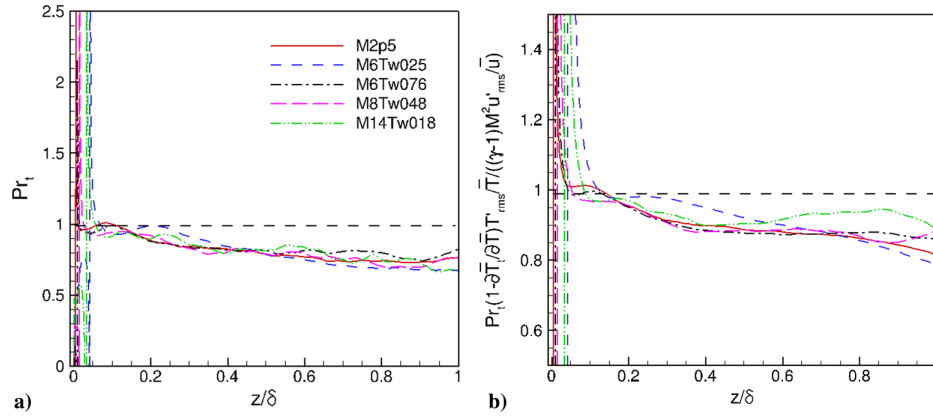
Fig. 9 a) Turbulent Prandtl number and b) Huang's modified SRA as a function of wall-normal distance.
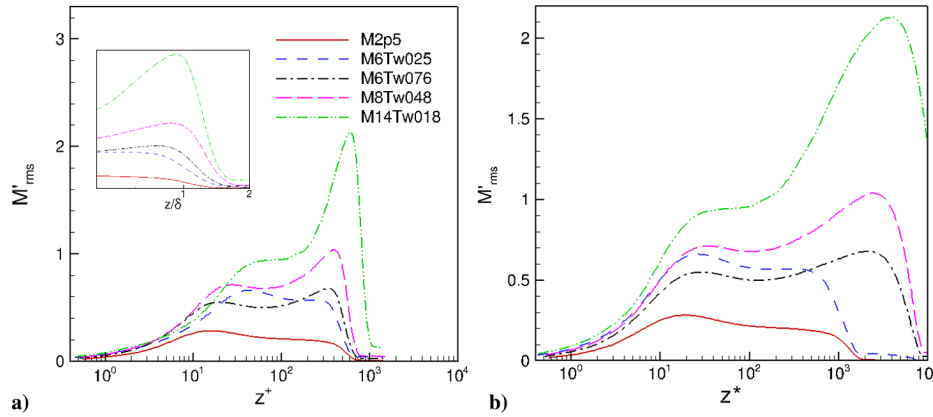

Fig. 10 Wall-normal distribution of fluctuating Mach number for various Mach number cases, with the wall-normal distance nondimensionalized by a) wall units and b) semilocal units.

Figures 10a and 10b plot the simulation results of the wall-normal variation of the fluctuating Mach number M'_{rms}, with the wall-normal distance nondimensionalized by wall units and semilocal units, respectively. The fluctuating Mach number increases dramatically with the freestream Mach number, and such an increase cannot be accounted for with the semilocal scaling. At Mach 7.87 and 13.64, the fluctuating Mach number develops a strong peak with a peak value greater than one toward the edge of the boundary layer. As a result, the turbulent fluctuations become locally supersonic relative to the surrounding flow, likely creating local shocklets that may be the source of significant dilatational dissipation and entropy production. Figures 11a and 11b further show that the peak of M'_{rms} at the boundary-layer edge is associated with the strong local fluctuations of density and temperature. The sharp gradients of the density and temperature at the boundary-layer edge may be connected with the turbulent-nonturbulent interface or the edge of the turbulent bulges as illustrated in Fig. 12. Unlike the r.m.s. profiles of density and temperature from Figs. 11a and 11b, the profile of r.m.s. pressure fluctuations (Fig. 11c) does not exhibit a strong peak near the edge of the boundary layer. The different behavior of the density and temperature fluctuations in comparison with the pressure fluctuations as well as the similarity in the density and temperature magnitudes near the edge of the boundary layer may be indicative of the local importance of the entropic mode. Indeed, as shown by Fig. 11d, the entropy fluctuation profile exhibits a local peak near the boundary-layer edge, similar to that of density and temperature fluctuations. The peak in entropy may be the result of enhanced heat conduction due to rapid variation in unsteady temperature profile that acts as a strong local source of entropy spots. The entropy fluctuations decay rapidly outside the boundary layer. For $z/\delta \geq 1.6$, the acoustic mode becomes dominant due to "eddy-Mach-wave" radiation from the boundary layer [53]. The acoustic radiation increases significantly with increasing freestream Mach number as reported in Refs. [32–34].

C. Reynolds Stress Anisotropy

Figure 13 plots the Reynolds stress anisotropy for the various Mach number cases. The anisotropy tensor is defined as

$$b_{ij} = \frac{\overline{\rho u_i'' u_j''}}{2\overline{\rho}\tilde{k}} - \frac{1}{3}\delta_{ij} \qquad (4)$$

The semilocal scaling is successful in collapsing the near-wall peak locations of the normal and shear stress anisotropies among the DNS cases. Of the three normal components of anisotropy, the streamwise component b_{11} increases with increasing Mach number and wall cooling for $z^* \geq 10$, whereas the opposite is seen for the spanwise component b_{22}. As discussed by Patel et al. [9,10] and Duan et al. [26], the increase in b_{11} with increasing Mach number and wall-cooling rate may indicate a decrease in the redistribution of turbulent energy from the streamwise direction to the other two directions when the Mach number and wall-cooling rate increase. The decreased redistribution of turbulent energy is also consistent with the increased peak value of u'_{rms}/u^* (Fig. 5b) when the Mach number and wall cooling rate are increased.

Compared with b_{11} and b_{22}, the wall-normal component of the normal stress anisotropy, b_{33}, and the Reynolds shear stress anisotropy, b_{13}, are less sensitive to Mach number and wall-cooling conditions, with the influence of Mach number and wall cooling limited to $z^* \lesssim 10$.

D. Turbulent Kinetic Energy Budget

The turbulent kinetic energy (TKE) for a compressible boundary layer is given by

$$\frac{D(\bar{\rho}\tilde{k})}{Dt} = P + TT + \Pi - \phi + D + ST \qquad (5)$$
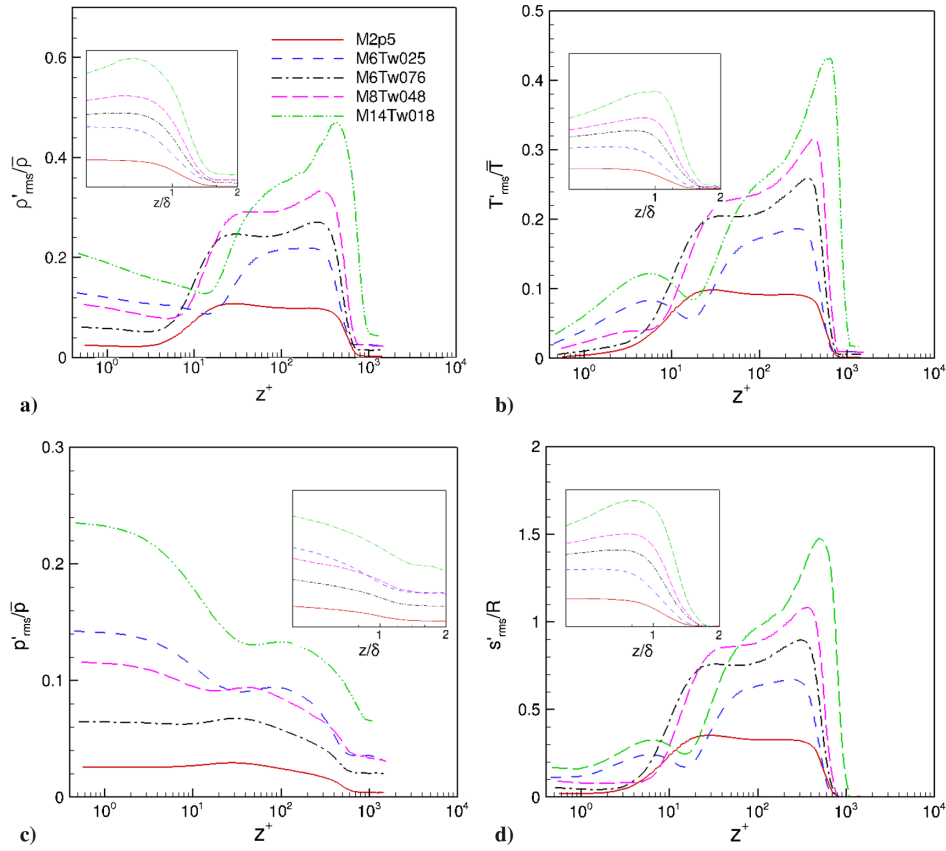
Fig. 11   Wall-normal distribution of the r.m.s. fluctuations of a) density, b) temperature, c) pressure, and d) entropy for various Mach number cases.
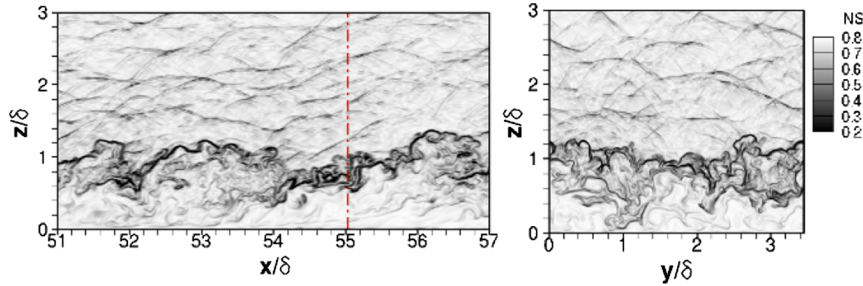

Fig. 12   Visualization of a typical instantaneous flow field for case M14Tw018 in a streamwise wall-normal (x–z) plane and a spanwise wall-normal (y–z) plane. The contours are those of numerical schlieren, with density gradient contour levels selected to emphasize large-scale motions of the boundary layer. The location of the y–z plane is indicated by the vertical dashed line.

with

$$P = -\overline{\rho u_i'' u_k''} \frac{\partial \widetilde{u}_i}{\partial x_k}$$

$$TT = -\frac{\partial}{\partial x_k}\left(\frac{1}{2}\overline{\rho u_i'' u_i'' u_k''}\right)$$

$$\Pi = \Pi^t + \Pi^d = -\frac{\partial}{\partial x_i}(\overline{p' u_i''}) + \overline{p'\frac{\partial u_i''}{\partial x_i}}$$

$$\phi = \overline{\tau_{ik}'\frac{\partial u_i''}{\partial x_k}}$$

$$D = \frac{\partial}{\partial x_k}(\overline{\tau_{ik}'' u_i''})$$

$$ST = \overline{u_i''}\left(\frac{\partial \bar{\tau}_{ik}}{\partial x_k} - \frac{\partial \bar{p}}{\partial x_i}\right) - \bar{\rho}\,\tilde{k}\frac{\partial \tilde{u}_k}{\partial x_k} \qquad (6)$$

where P is the production term, TT is the turbulent transport term, Π is the pressure term (pressure diffusion and pressure dilatation), $-\phi$ is

viscous dissipation per unit volume, D is viscous diffusion, and ST represents additional terms that arise when density is not constant.

Figure 14 plots the terms in the TKE budget, normalized by the conventional inner scaling (Fig. 14a) and the "semilocal" scaling (Fig. 14b). The additional terms arising due to density variation (ST) have a negligible variation compared with the other terms and are thus excluded from the figure. Overall, the semilocal scaling yields a significantly better collapse of the budget terms among the different Mach number cases in comparison with the inner scaling. Such a finding is consistent with the previous study by Duan et al. [25,26] based on temporal DNS of turbulent boundary layers up to Mach 12. Figure 15 further shows that the semilocal scaling largely collapses the terms associated with turbulence production, turbulence transport, pressure terms, and viscous diffusion and dissipation. Notable differences among the different cases are confined to the inner region with $z^* \lesssim 5$. The production term shows a near-wall peak in the buffer layer at $z^* \approx 12$ with a slight increase in the peak value as the Mach number increases. The collapse of the near-wall peak in the buffer layer and the increase in the peak value with Mach number are consistent with those of the Morkovin-transformed streamwise turbulence intensity u_{rms}'/u^*.
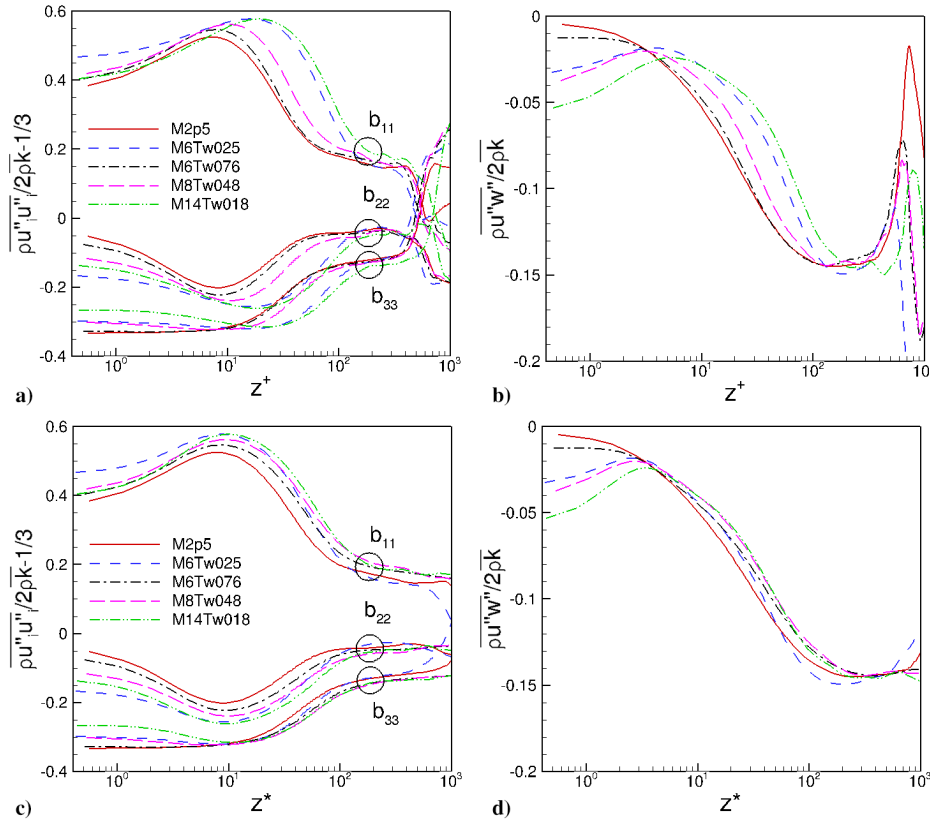
Fig. 13   Distributions of normal Reynolds stress anisotropies (a, c) and Reynolds shear stress anisotropy (b, d). Open circles are used to group the various cases for each normal stress component in (a) and (c), and hence to make the profiles for different components easier to distinguish from each other. The anisotropy tensor is defined as $b_{ij} = \overline{\rho u_i'' u_j''}/2\overline{\rho k} - \delta_{ij}/3$.
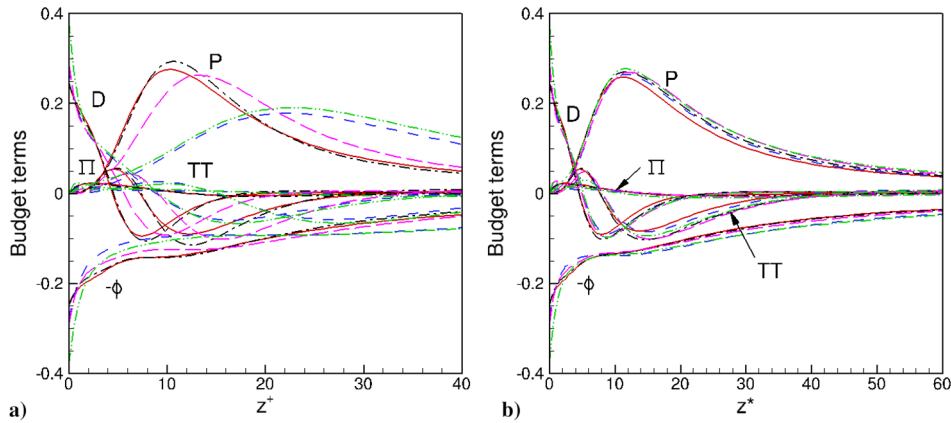
Fig. 14   TKE budget for different cases nondimensionalized by a) wall units and b) semilocal units, respectively. Variables in wall units are normalized by $\bar{\rho}_w u_\tau^3/z_\tau$, and variables in semilocal units are normalized by $\bar{\rho} u^{*3}/z_\tau^*$. Solid lines, M2p5; dashed lines, M6Tw025; dash-dot lines, M6Tw076; long dash lines, M8Tw048; dash-dot-dot lines, M14Tw018.

The effects of compressibility on the dissipation have been of interest in the context of compressible turbulence models [54–56]. The dissipation can be expanded into solenoidal dissipation ϕ_s and dilatational dissipation ϕ_d, after neglecting terms that involve viscosity fluctuations and the term due to inhomogeneity [6,36]. Figure 16 plots the wall-normal variation in solenoidal and dilatational components of the dissipation rate. The solenoidal dissipation ϕ_s normalized with semilocal units is insensitive to Mach number and wall temperature conditions, except in the near-wall region of $z^* \lesssim 10$ (Fig. 16a), whereas the dilatational dissipation increases significantly with increasing freestream Mach number or wall-cooling rate (Fig. 16b). At $M_\infty = 13.64$, the dilatational dissipation ϕ_d becomes non-negligible compared with the solenoidal dissipation ϕ_s, with a maximal ratio of $\phi_d/\phi_s \approx 11\%$ in regions near the wall and close to the boundary-layer edge (Fig. 16c). Both the

dilatational dissipation and the solenoidal dissipation become insignificant near the boundary-layer edge; the increase in the ratio of ϕ_d/ϕ_s toward the boundary-layer edge is largely caused by a faster decay of the solenoidal dissipation compared with that of the dilatational dissipation. The small values of dilatational dissipation near the boundary-layer edge may suggest that the formation of shocklets, as indicated by strong localized density gradient in instantaneous flow visualizations (Fig. 12) and the supersonic fluctuating Mach number (Fig. 10a), is infrequent enough for the shocklets to have any appreciable influence on the dilatational dissipation, at least for the cases studied.

Finally, the effect of compressibility on the pressure terms is considered. The pressure terms for a compressible flow include pressure diffusion (Π^t), pressure dilatation (Π^d), and compressibility (Π^c), defined as
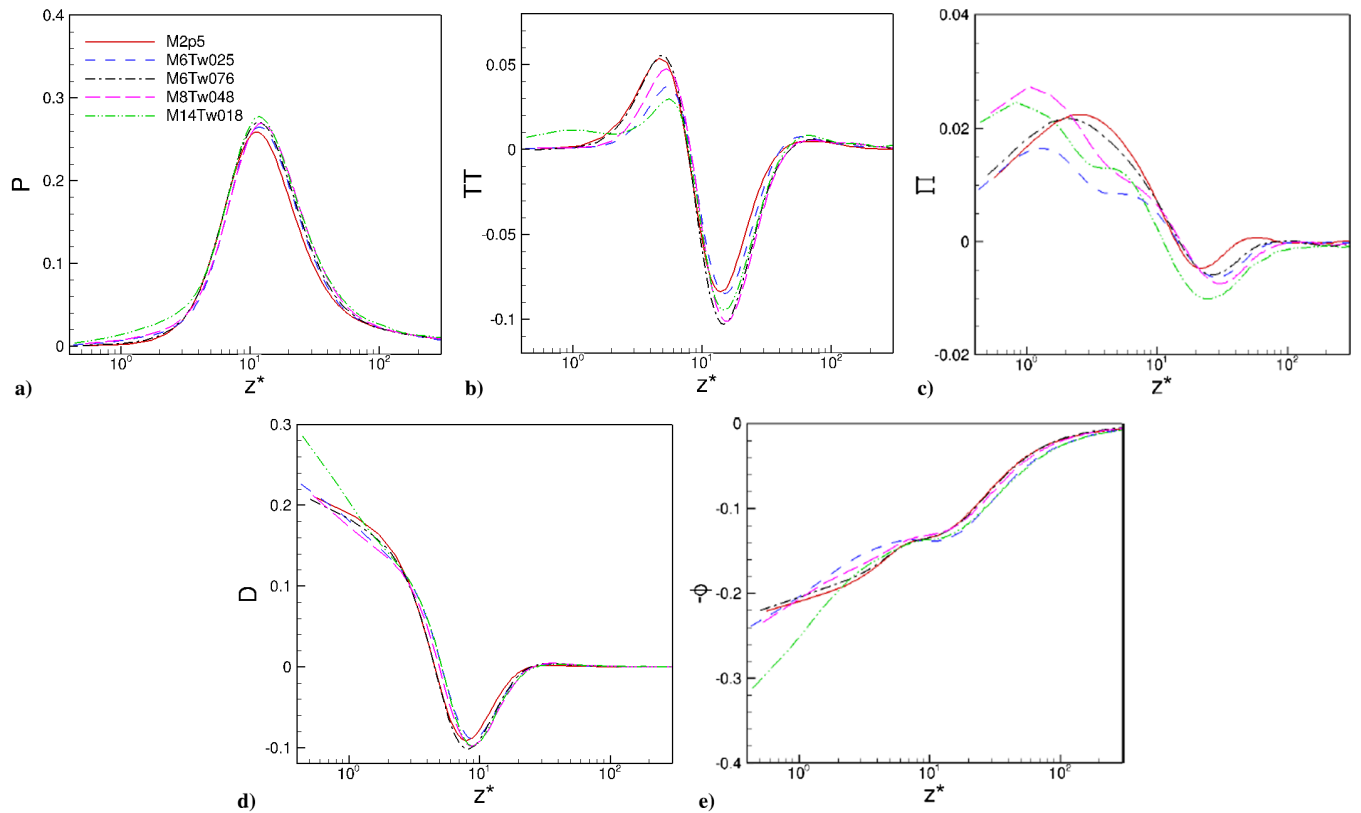
Fig. 15   TKE budget terms for different cases normalized by $\bar{\rho} u^{*3}/z_\tau^*$.
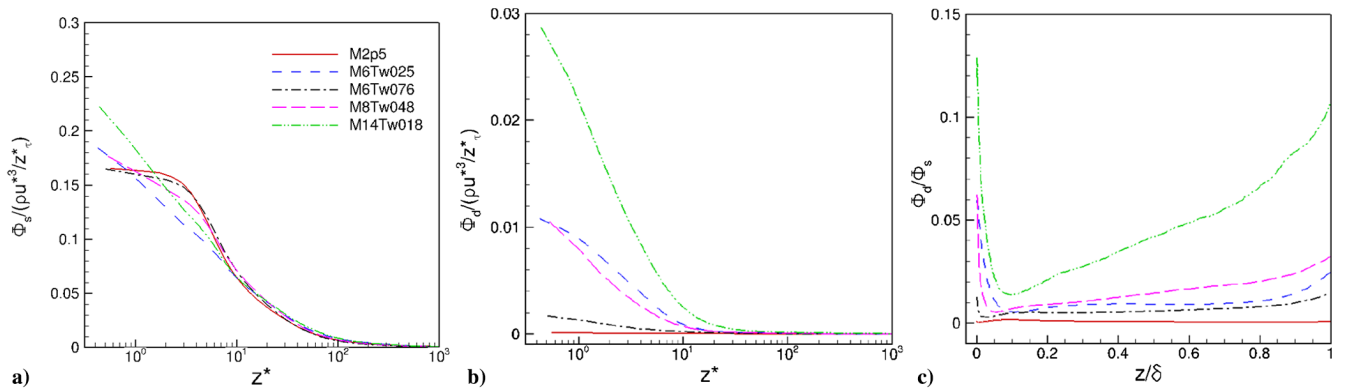

Fig. 16   Plot of solenoidal dissipation $\phi_s = \bar{\mu}\,\overline{\omega_i'\omega_i'}$ and dilatational dissipation $\phi_d = 4/3\bar{\mu}\,\overline{(\partial u_i'/\partial x_i)(\partial u_k'/\partial x_k)}$ as a function of wall-normal distance.
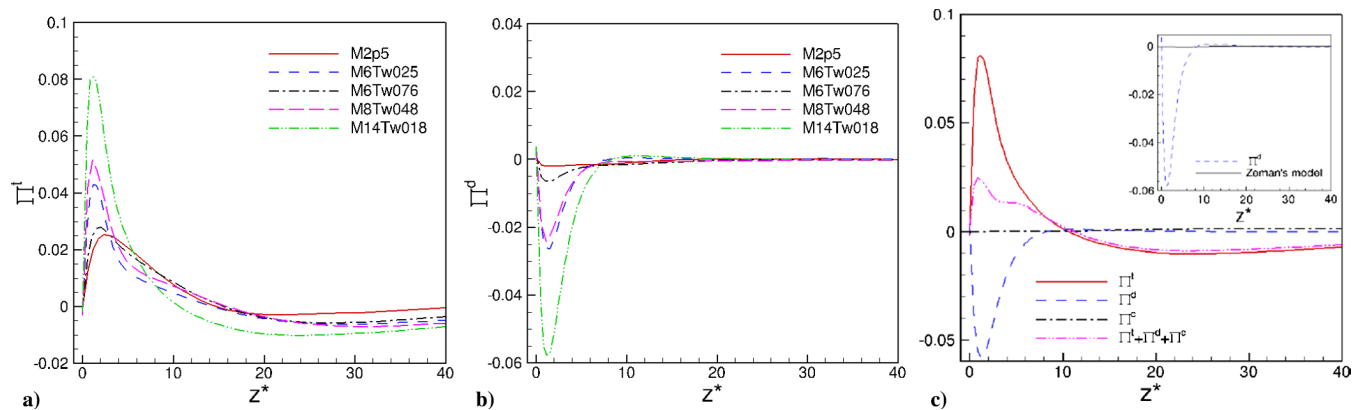

Fig. 17   Wall-normal variation of pressure terms: a) pressure diffusion and b) pressure dilatation for the various DNS cases; c) comparison of pressure terms for case M14Tw018. All the terms are normalized by $\bar{\rho} u^{*3}/z_\tau^*$. For comparison, the Zeman's compressibility correction [30], defined as $\Pi^d = 0.02\gamma[1 - \exp(-M_t^2/0.2)]\bar{p}\,\overline{u_i''}(\partial \bar{\rho}/\partial x_i)/\bar{\rho}$, is also plotted in (c).

$$\Pi^t = -\frac{\partial}{\partial x_i}(\overline{p'u_i''}), \quad \Pi^d = \overline{p'\frac{\partial u_i''}{\partial x_i}}, \quad \Pi^c = -\overline{u_i''}\frac{\partial \bar{p}}{\partial x_i} \quad (7)$$

Figures 17a and 17b show comparisons of pressure diffusion and pressure dilatation, respectively, among the various DNS cases. The pressure diffusion and pressure dilatation terms show a large Mach number and wall temperature dependence, especially in the near wall region ($z^* \lesssim 10$). The pressure dilatation Π^d increases with Mach number, and at Mach 13.64, the pressure dilatation term has significant contribution to the sum of the pressure terms in the wall region with $z^* \lesssim 10$ (Fig. 17c). The Zeman compressibility correction is insufficient for correcting Π^d for $z^* \lesssim 10$. However, it conforms well with the DNS farther away from the wall. Although not shown here, the traditional Sarkar–Zeman–Wilcox correction for free-shear flows [54–56] significantly overcorrects throughout the boundary layer when applied to the current DNS cases. The better match of Zeman's model with the DNS is consistent with the observation by Rumsey [31], who showed that Zeman's compressibility correction exhibits a less dramatic influence than the free-shear type of correction when applied to boundary-layer flows, and that the correction works reasonably well in predicting wall skin friction for cold-wall cases. As also indicated by Fig. 17c, Π^c is negligibly small in comparison with Π^t and Π^d throughout the boundary layer.

IV. Conclusions

A direct numerical simulations (DNS) database of high-speed, zero-pressure-gradient turbulent boundary layers developing spatially over a flat plate is presented. Complementary to the limited datasets in the literature under high Mach number, cold-wall conditions, the database covers a wide range of freestream Mach numbers ($M_\infty = 2.5$–14) and wall-to-recovery temperature ratios ($T_w/T_r = 0.18$–1.0) and simulates the operational conditions of hypervelocity wind tunnels. The DNS is based on a high-order scheme with a large domain size and sufficiently long sampling size ($L_x/\delta_i > 50$, $L_y/\delta_i > 8$, $T_f u_\tau/\delta_i > 5$) to minimize any artificial effects due to inflow turbulence generation and to ensure the convergence of some of the high-order turbulence statistics. The physical realism and accuracy of the computed flow fields have been established by comparing with existing experimental results at similar flow conditions and with other high-quality simulations at lower Mach numbers.

The DNS database has been used to gauge the performance of compressibility transformations in the high-Mach-number, cold-wall regime, including the recently developed velocity and temperature scalings that explicitly account for the effect of wall cooling, with the main observations and conclusions summarized as follows:

1) The mean velocity transformation of Trettel and Larsson [7] yields much improved collapse of the hypersonic data in the viscous sublayer when there is a strong heat transfer at the surface.

2) Zhang's generalized relation [8] between the mean velocity and the mean temperature yields better comparison with the DNS than that of Walz under cold wall conditions.

3) The semilocal scaling successfully collapses the Reynolds stresses, vorticity fluctuations, and the turbulent kinetic energy (TKE) budgets in most of the boundary layer at different Mach number and wall-cooling conditions, with notable differences largely limited to the near-wall region ($z^* \lesssim 10$).

The apparent success of the various compressibility transformations in most of the boundary layer indicates that, within the relatively broad range of Mach number and wall cooling considered in this study, the effects of those two parameters can be largely taken into account with local mean flow conditions, in terms of density and viscosity, and that the turbulence dynamics of hypersonic turbulent boundary layers exhibits strong similarity to that of incompressible flows at comparable Reynolds numbers.

Additional insights into the effects of intrinsic compressibility and wall-cooling are gained from the inspection of Reynolds stress anisotropy, the thermodynamic fluctuations, and the dissipation and

pressure terms in TKE budgets. The main observations may be summarized as follows:

1) There is an increase in the streamwise component of the Reynolds stress anisotropy and a decrease in the spanwise component as the Mach number and wall cooling increase, and such a change in Reynolds stress anisotropy may be indicative of modifications to intercomponent energy transfer in the high-Mach-number, cold-wall regime.

2) The fluctuating Mach number increases dramatically with the freestream Mach number, and at Mach 7.87 and 13.64, turbulent fluctuations become locally supersonic relative to the surrounding flow near the edge of the boundary layer.

3) As a result of the locally supersonic turbulent bulges and the likely creation of local shocklets that are a source of significant entropy production and dilatational dissipation, the fluctuating density and temperature develop a strong peak with large entropy fluctuations toward the edge of the boundary layer.

4) A sharp gradient in density and temperature is seen at the instantaneous interface between turbulent and nonturbulent flow regions or the edge of the turbulent bulges for the high-Mach-number cases.

5) The dilatational dissipation and the pressure dilatation increase dramatically with increasing Mach number and wall-cooling rate. At Mach 13.64, the dilatational dissipation becomes non-negligible compared with the solenoidal dissipation in the near-wall region and close to the boundary-layer edge; pressure dilatation has a significant contribution to the sum of the pressure terms in the near-wall region ($z^* \lesssim 10$) but the contribution diminishes farther away from the wall.

The DNS database under hypervelocity (but ideal gas) conditions complements the limited experimental datasets and the existing DNS databases that simulate either temporal boundary layers [23,25,26] or spatial boundary layers over an adiabatic wall [28]. The database therefore represents a reliable resource for studying turbulence physics under high Mach number, cold-wall conditions and for validating compressibility transformations and RANS models. Precomputed flow statistics including Reynolds stresses and their budgets will be available at the website of the NASA Langley Turbulence Modeling Resource,§ allowing other investigators to query any property of interest.

References

[1] Smits, A. J., and Dussauge, J. P., *Turbulent Shear Layers in Supersonic Flow*, 2nd ed., Springer–Verlag, New York, 2006, pp. 119–134.
doi:10.1007/b137383

[2] van Driest, E. R., "The Problem of Aerodynamic Heating," *Aeronautical Engineering Review*, Vol. 15, No. 10, 1956, pp. 26–41.

[3] Walz, A., *Boundary Layers of Flow and Temperature*, MIT Press, Cambridge, MA, 1969, pp. 27–75.

[4] Morkovin, M. V., "Effects of Compressibility on Turbulent Flows," *Mécanique de la Turbulence*, edited by A. J. Favre, CNRS, Paris, 1962, pp. 367–380.

[5] Gaviglio, J., "Reynolds Analogies and Experimental Study of Heat Transfer in the Supersonic Boundary Layer," *International Journal of Heat and Mass Transfer*, Vol. 30, No. 5, 1987, pp. 911–926.
doi:10.1016/0017-9310(87)90010-X

[6] Huang, P. G., Coleman, G., and Bradshaw, P., "Compressible Turbulent Channel Flows: DNS Results and Modelling," *Journal of Fluid*

Mechanics, Vol. 305, Dec. 1995, pp. 185–218.
doi:10.1017/S0022112095004599

[7] Trettel, A., and Larsson, J., "Mean Velocity Scaling for Compressible Wall Turbulence with Heat Transfer," *Physics of Fluids*, Vol. 28, No. 2, 2016, Paper 026102.
doi:10.1063/1.4942022

[8] Zhang, Y., Bi, W., Hussain, F., and She, Z., "A Generalized Reynolds Analogy for Compressible Wall-Bounded Turbulent Flows," *Journal of Fluid Mechanics*, Vol. 739, Jan. 2014, pp. 392–420.
doi:10.1017/jfm.2013.620

[9] Patel, A., Boersma, B. J., and Pecnik, R., "The Influence of Near-Wall Density and Viscosity Gradients on Turbulence in Channel Flows," *Journal of Fluid Mechanics*, Vol. 809, Dec. 2016, pp. 793–820.
doi:10.1017/jfm.2016.689

[10] Patel, A., Peeters, J. W., Boersma, B. J., and Pecnik, R., "Semi-Local Scaling and Turbulence Modulation in Variable Property Turbulent Channel Flows," *Physics of Fluids*, Vol. 27, No. 9, 2015, Paper 095101.
doi:10.1063/1.4929813

[11] Modesti, D., and Pirozzoli, S., "Reynolds and Mach Number Effects in Compressible Turbulent Channel Flow," *International Journal of Heat and Fluid Flow*, Vol. 59, June 2016, pp. 33–49.
doi:10.1016/j.ijheatfluidflow.2016.01.007

[12] Roy, C. J., and Blottner, F. G., "Review and Assessment of Turbulence Models for Hypersonic Flows," *Progress in Aerospace Sciences*, Vol. 42, Nos. 7–8, 2006, pp. 469–530.
doi:10.1016/j.paerosci.2006.12.002

[13] Williams, O. J. H., Sahoo, D., Baumgartner, M. L., and Smits, A. J., "Experiments on the Structure and Scaling of Hypersonic Turbulent Boundary Layers," *Journal of Fluid Mechanics*, Vol. 834, Jan. 2018, pp. 237–270.
doi:10.1017/jfm.2017.712

[14] Kovasznay, L. S., "Turbulence in Supersonic Flow," *Journal of the Aeronautical Sciences*, Vol. 20, No. 10, 1953, pp. 657–674.
doi:10.2514/8.2793

[15] Ekoto, I. W., Bowersox, R. D. W., Brutner, T., and Goss, L., "Supersonic Boundary Layers with Periodic Surface Roughness," *AIAA Journal*, Vol. 46, No. 2, 2008, pp. 486–497.
doi:10.2514/1.31729

[16] Tichenor, N. R., Humble, R. A., and Bowersox, R. D. W., "Response of a Hypersonic Turbulent Boundary Layer to Favourable Pressure Gradients," *Journal of Fluid Mechanics*, Vol. 722, May 2013, pp. 187–213.
doi:10.1017/jfm.2013.89

[17] Peltier, S., Humble, R., and Bowersox, R., "Crosshatch Roughness Distortions on a Hypersonic Turbulent Boundary Layer," *Physics of Fluids*, Vol. 28, No. 4, 2016, Paper 045105.
doi:10.1063/1.4944657

[18] Maeder, T., "Numerical Investigation of Supersonic Turbulent Boundary Layers," Ph.D. Thesis, ETH, Zürich, 2000.

[19] Shahab, M. F., Lehnasch, G., Gatski, T. B., and Comte, P., "Statistical Characteristics of an Isothermal, Supersonic Developing Boundary Layer Flow from DNS Data," *Flow, Turbulence and Combustion*, Vol. 86, Nos. 3–4, 2011, pp. 369–397.
doi:10.1007/s10494-011-9329-0

[20] Hadjadj, A., Ben-Nasr, O., Shadloo, M., and Chaudhuri, A., "Effect of Wall Temperature in Supersonic Turbulent Boundary Layers: A Numerical Study," *International Journal of Heat and Mass Transfer*, Vol. 81, Feb. 2015, pp. 426–438.
doi:10.1016/j.ijheatmasstransfer.2014.10.025

[21] Pirozzoli, S., and Bernardini, M., "Turbulence in Supersonic Boundary Layers at Moderate Reynolds Numbers," *Journal of Fluid Mechanics*, Vol. 688, Dec. 2011, pp. 120–168.
doi:10.1017/jfm.2011.368

[22] Poggie, J., Bisek, N. J., and Gosse, R., "Resolution Effects in Compressible, Turbulent Boundary Layer Simulations," *Computers and Fluids*, Vol. 120, Oct. 2015, pp. 57–69.
doi:10.1016/j.compfluid.2015.07.015

[23] Martín, M. P., "DNS of Hypersonic Turbulent Boundary Layers," *34th AIAA Fluid Dynamics Conference and Exhibit*, AIAA Paper 2004-2337, June 2004.
doi:10.2514/6.2004-2337

[24] Martín, M., "DNS of Hypersonic Turbulent Boundary Layers. Part I: Initialization and Comparison with Experiments," *Journal of Fluid Mechanics*, Vol. 570, Jan. 2007, pp. 347–364.
doi:10.1017/S0022112006003107

[25] Duan, L., Beekman, I., and Martín, M. P., "Direct Numerical Simulation of Hypersonic Turbulent Boundary Layers. Part 3: Effect of Mach Number," *Journal of Fluid Mechanics*, Vol. 672, April 2011, pp. 245–267.
doi:10.1017/S0022112010005902

[26] Duan, L., Beekman, I., and Martín, M. P., "Direct Numerical Simulation of Hypersonic Turbulent Boundary Layers. Part 2: Effect of Wall Temperature," *Journal of Fluid Mechanics*, Vol. 655, July 2010, pp. 419–445.
doi:10.1017/S0022112010000959

[27] Duan, L., and Martín, M. P., "Direct Numerical Simulation of Hypersonic Turbulent Boundary Layers. Part 4: Effect of High Enthalpy," *Journal of Fluid Mechanics*, Vol. 684, Oct. 2011, pp. 25–59.
doi:10.1017/jfm.2011.252

[28] Lagha, M., Kim, J., Eldredge, J., and Zhong, X., "A Numerical Study of Compressible Turbulent Boundary Layers," *Physics of Fluids*, Vol. 23, No. 1, 2011, Paper 015106.
doi:10.1063/1.3541341

[29] Priebe, S., and Martín, M. P., "Direct Numerical Simulation of a Hypersonic Turbulent Boundary Layer on a Large Domain," *41st AIAA Fluid Dynamics Conference and Exhibit*, AIAA Paper 2011-3432, June 2011.
doi:10.2514/6.2011-3432

[30] Zeman, O., "A New Model for Supersonic/Hypersonic Turbulent Boundary Layers," *31st Aerospace Sciences Meeting*, AIAA Paper 1993-0897, Jan. 1993.
doi:10.2514/6.1993-897

[31] Rumsey, C. L., "Compressibility Considerations for $k-\omega$ Turbulence Models in Hypersonic Boundary-Layer Applications," *Journal of Spacecraft and Rockets*, Vol. 47, No. 1, 2010, pp. 11–20.
doi:10.2514/1.45350

[32] Duan, L., Choudhari, M. M., and Wu, M., "Numerical Study of Pressure Fluctuations Due to a Supersonic Turbulent Boundary Layer," *Journal of Fluid Mechanics*, Vol. 746, May 2014, pp. 165–192.
doi:10.1017/jfm.2014.116

[33] Duan, L., Choudhari, M. M., and Zhang, C., "Pressure Fluctuations Induced by a Hypersonic Turbulent Boundary Layer," *Journal of Fluid Mechanics*, Vol. 804, Oct. 2016, pp. 578–607.
doi:10.1017/jfm.2016.548

[34] Zhang, C., Duan, L., and Choudhari, M. M., "Effect of Wall Cooling on Boundary Layer Induced Pressure Fluctuations at Mach 6," *Journal of Fluid Mechanics*, Vol. 822, July 2017, pp. 5–30.
doi:10.1017/jfm.2017.212

[35] Zhang, C., Duan, L., and Choudhari, M. M., "Acoustic Radiation from a Mach 14 Turbulent Boundary Layers," *54th AIAA Aerospace Sciences Meeting*, AIAA Paper 2016-0048, Jan. 2016.
doi:10.2514/6.2016-0048

[36] Guarini, S. E., Moser, R. D., Shariff, K., and Wray, A., "Direct Numerical Simulation of a Supersonic Turbulent Boundary Layer at Mach 2.5," *Journal of Fluid Mechanics*, Vol. 414, July 2000, pp. 1–33.
doi:10.1017/S0022112000008466

[37] Duan, L., Choudhari, M. M., Chou, A., Munoz, F., Ali, S. R. C., Radespiel, R., Schilden, T., Schröder, W., Marineau, E. C., and Casper, K. M., et al., "Characterization of Freestream Disturbances in Conventional Hypersonic Wind Tunnels," *2018 AIAA Aerospace Sciences Meeting, AIAA SciTech Forum*, AIAA Paper 2018-0347, Jan. 2018.
doi:10.2514/6.2018-0347

[38] Shadloo, M., Hadjadj, A., and Hussain, F., "Statistical Behavior of Supersonic Turbulent Boundary Layers with Heat Transfer at $M_\infty = 2$," *International Journal of Heat and Fluid Flow*, Vol. 53, June 2015, pp. 113–134.
doi:10.1016/j.ijheatfluidflow.2015.02.004

[39] Smits, A. J., and Martín, M. P., "Turbulence in Supersonic and Hypersonic Boundary Layers," *IUTAM Symposium on One Hundred Years of Boundary Layer Research*, DLR Göttingen, Germany, Aug. 2004, pp. 221–230.

[40] Lele, S. K., "Compressibility Effects on Turbulence," *Annual Review of Fluid Mechanics*, Vol. 26, No. 1, 1994, pp. 211–254.
doi:10.1146/annurev.fl.26.010194.001235

[41] Keyes, F. G., "A Summary of Viscosity and Heat-Conduction Data for He, A, H_2, O_2, CO, CO_2, H_2O, and Air," *Transactions of the American Society of Mechanical Engineers*, Vol. 73, July 1951, pp. 589–596.

[42] Martín, M. P., Taylor, E. M., Wu, M., and Weirs, V. G., "A Bandwidth-Optimized WENO Scheme for the Direct Numerical Simulation of Compressible Turbulence," *Journal of Computational Physics*, Vol. 220, No. 1, 2006, pp. 270–289.
doi:10.1016/j.jcp.2006.05.009

[43] Taylor, E. M., Wu, M., and Martín, M. P., "Optimization of Nonlinear Error Sources for Weighted Non-Oscillatory Methods in Direct Numerical Simulations of Compressible Turbulence," *Journal of Computational Physics*, Vol. 223, No. 1, 2007, pp. 384–397.
doi:10.1016/j.jcp.2006.09.010

[44] Williamson, J., "Low-Storage Runge-Kutta Schemes," *Journal of Computational Physics*, Vol. 35, No. 1, 1980, pp. 48–56.
doi:10.1016/0021-9991(80)90033-9

[45] Duan, L., and Choudhari, M. M., "Analysis of Numerical Simulation Database for Pressure Fluctuations Induced by High-Speed Turbulent Boundary Layers," *20th AIAA/CEAS Aeroacoustics Conference, AIAA AVIATION Forum*, AIAA Paper 2014-2912, 2014.
doi:10.2514/6.2014-2912

[46] Wu, B., Bi, W., Hussain, F., and She, Z.-S., "On the Invariant Mean Velocity Profile for Compressible Turbulent Boundary Layers," *Journal of Turbulence*, Vol. 18, No. 2, 2016, pp. 1–17.
doi:10.1080/14685248.2016.1269911

[47] Coleman, G. N., Kim, J., and Moser, R. D., "A Numerical Study of Turbulent Supersonic Isothermal-Wall Channel Flow," *Journal of Fluid Mechanics*, Vol. 305, Dec. 1995, pp. 159–183.
doi:10.1017/S0022112095004587

[48] Foysi, H., Sarkar, S., and Friedrich, R., "Compressibility Effects and Turbulence Scalings in Supersonic Channel Flow," *Journal of Fluid Mechanics*, Vol. 509, June 2004, pp. 207–216.
doi:10.1017/S0022112004009371

[49] Degraaff, D. B., and Eaton, J. K., "Reynolds-Number Scaling of the Flat-Plate Turbulent Boundary Layer," *Journal of Fluid Mechanics*, Vol. 422, Nov. 2000, pp. 319–346.
doi:10.1017/S0022112000001713

[50] Sillero, J. A., Jiménez, J., and Moser, R. D., "One-Point Statistics for Turbulent Wall-Bounded Flows at Reynolds Numbers up to $\delta^+ \approx 2000$," *Physics of Fluids*, Vol. 25, No. 10, 2013, Paper 105102.
doi:10.1063/1.4823831

[51] Jiménez, J., Hoyas, S., Simens, M. P., and Mizuno, Y., "Turbulent Boundary Layers and Channels at Moderate Reynolds Numbers," *Journal of Fluid Mechanics*, Vol. 657, Aug. 2010, pp. 335–360.
doi:10.1017/S0022112010001370

[52] Bernardini, M., and Pirozzoli, S., "Wall Pressure Fluctuations Beneath Supersonic Turbulent Boundary Layers," *Physics of Fluids*, Vol. 23, No. 8, 2011, Paper 085102.
doi:10.1063/1.3622773

[53] Laufer, J., "Some Statistical Properties of the Pressure Field Radiated by a Turbulent Boundary Layer," *Physics of Fluids*, Vol. 7, No. 8, 1964, pp. 1191–1197.
doi:10.1063/1.1711360

[54] Zeman, O., "Dilatation Dissipation: The Concept and Application in Modeling Compressible Mixing Layers," *Physics of Fluids A*, Vol. 2, No. 2, 1990, pp. 178–188.
doi:10.1063/1.857767

[55] Sarkar, S., Erlebacher, G., Hussaini, M. Y., and Kreiss, H. O., "The Analysis and Modeling of Dilatational Terms in Compressible Turbulence," *Journal of Fluid Mechanics*, Vol. 227, June 1991, pp. 473–493.
doi:10.1017/S0022112091000204

[56] Wilcox, D. C., *Turbulence Modeling for CFD*, 3rd ed., DCW Industries, Glendale, CA, 2006, pp. 257–259.